• Data Description Article •

Eddy-resolving Simulation of CAS-LICOM3 for Phase 2 of the Ocean Model Intercomparison Project

Yiwen LI[1,2], Hailong LIU[1,2], Mengrong DING[1,2], Pengfei LIN[*1,2], Zipeng YU[1,2], Yongqiang YU[1,2],
Yao MENG[1,2], Yunlong LI[3], Xiaodong JIAN[3], Jinrong JIANG[4], Kangjun CHEN[1],
Qian YANG[1,2], Yaqi WANG[1,2], Bowen ZHAO[1,2], Jilin WEI[1,2],
Jinfeng MA[1], Weipeng ZHENG[1,2], and Pengfei WANG[1]

[1]*State Key Laboratory of Numerical Modeling for Atmospheric Sciences and Geophysical Fluid Dynamics*,
Institute of Atmospheric Physics, *Chinese Academy of Sciences*, *Beijing* 100029, *China*
[2]*College of Earth and Planetary Sciences*, *University of Chinese Academy of Sciences*, *Beijing* 100049, *China*
[3]*National Supercomputer Center in Tianjin*, *Tianjin* 300457, *China*
[4]*Computer Network Information Center*, *Chinese Academy of Sciences*, *Beijing* 100190, *China*

ABSTRACT

A 61-year (1958–2018) global eddy-resolving dataset for phase 2 of the Ocean Model Intercomparison Project has been produced by the version 3 of Chinese Academy of Science, the State Key Laboratory of Numerical Modeling for Atmospheric Sciences and Geophysical Fluid Dynamics/Institute of Atmospheric Physics (LASG/IAP) Climate system Ocean Model (CAS-LICOM3). The monthly and a part of the surface daily data in this study can be accessed on the Earth System Grid Federation (ESGF) node. Besides the details of the model and experiments, the evolutions and spatial patterns of large-scale and mesoscale features are also presented. The mesoscale features are reproduced well in the high-resolution simulation, as the mesoscale activities can contribute up to 50% of the total SST variability in eddy-rich regions. Also, the large-scale circulations are remarkably improved compared with the low-resolution simulation, such as the climatological annual mean SST (the RMSE is reduced from 0.59°C to 0.47°C, globally) and the evolution of Atlantic Meridional Overturning Circulation. The preliminary evaluation also indicates that there are systematic biases in the salinity, the separation location of the western boundary currents, and the magnitude of eddy kinetic energy. All these biases are worthy of further investigation.

Key words: eddy-resolving dataset, mesoscale eddies, CAS-LICOM3, OMIP

---

1. Background and Summary

To understand the origin of model biases in phase 6 of the Coupled Model Intercomparison Project (CMIP6), the Ocean Model Intercomparison Project (OMIP; Griffies et al., 2016) was proposed to trace the coupled model biases in ocean–sea-ice models. Recently, the protocol of OMIP has been updated and two kinds of OMIP experiments forced by two different datasets have been proposed. Phase 1 of OMIP (OMIP-1) is forced by the CORE-II dataset (Large and Yeager, 2009), mainly derived from the NCEP–NCAR atmospheric reanalysis (Kalnay et al., 1996; Kistler et al., 2001), and phase 2 of OMIP (OMIP-2) is forced by the JRA55-do dataset (Tsujino et al., 2018), based on the Japanese 55-year Reanalysis (JRA-55; Kobayashi et al., 2015) and river runoff.

The results of OMIP-1 and OMIP-2 from 11 state-of-the-art global low-resolution ocean–sea-ice models were evaluated by Tsujino et al. (2020). Some improvements to key features were identified from the comparison, such as the attenuation of the warming biases off the eastern coast of the Pacific Ocean, as well the reproduction of the observed global warming and warming hiatus in the sea surface temperature (SST). However, some common model biases still persist, indicating errors in representing important processes or biases in the surface forcing. Among the possible causes, the horizontal resolution of the model is considered to be one of the important factors, particularly for the biases in eddy-rich regions, western boundary currents, and narrow straits. Therefore, additional OMIP-2 experiments using

---

global eddy-resolving ocean–sea-ice models were proposed and compared by Chassignet et al. (2020) to identify the robust improvements of ocean–sea-ice simulation by refining the model resolution from 100 km to 10 km.

Under the framework of this resolution-related comparison, four ocean modeling groups have conducted and submitted a pair of experiments: 100 km and 10 km versions of the model forced by the JRA55-do dataset for only one cycle (1958–2018). The experiments of the coarse resolution are just the same as the first cycle of OMIP-2 in Tsujino et al. (2020). The Chinese Academy of Science, State Key Laboratory of Numerical Modeling for Atmospheric Sciences and Geophysical Fluid Dynamics/Institute of Atmospheric Physics (LASG/IAP) Climate system Ocean Model, version 3 (CAS-LICOM3) is one of the models that has participated in the comparisons, which was developed based on the previous version, CAS-LICOM2 (Liu et al., 2012). CAS-LICOM3 is also the ocean component of FGOALS3, participating in CMIP6. The eddy-resolving simulation of CAS-LICOM3 for OMIP-2 (hereafter called CAS-LICOM3_High) was finished in November 2019 and the data submitted to the Earth System Grid Federation (ESGF) data server (https://esgf-node.llnl.gov/projects/cmip6/). Here, we document detailed information on the model configurations and experiments, as well as the results of diagnostic variables from CAS-LICOM3_High, to provide a general description of this dataset for a variety of users.

The organization of the paper is as follows. In section 2, we describe the ocean model, the experiment design, and the methods used here. Section 3 presents the basic technical validation of CAS-LICOM3_High. In this section, firstly, the temporal evolution of SST, sea surface salinity (SSS), Atlantic Meridional Overturning Circulation (AMOC), kinetic energy (KE), and upper-ocean temperature are presented for examining the trends and variabilities of the simulation. Secondly, the simulated spatial pattern and standard deviation (STD) of sea surface height (SSH) and SST are validated by splitting the large-scale signal and mesoscale eddies. Thirdly, the ocean surface currents are provided for showing the major currents, such as the western boundary currents and Antarctic Circumpolar Current (ACC). Finally, the North Equatorial Undercurrent (NEUC) is selected to evaluate this dataset, because it is a good indicator to examine the long-term and high-resolution simulation (Li et al., 2018). In section 4, the data record is described. Section 5 provides usage notes.

2. Model, experiment and methods

2.1. *Introduction to the model*

CAS-LICOM is a global ocean general circulation model developed by LASG/IAP of the Chinese Academy of Sciences (Zhang and Liang, 1989; Liu et al., 2004, 2012; Yu et al., 2018). CAS-LICOM3 is an ocean general circulation model with a free sea surface and Arakawa B grid, and uses the primitive equations with Boussinesq and hydro-

static approximations. It has been extensively upgraded since CAS-LICOM2. First, the coordinates of the dynamical core have been replaced by arbitrary orthogonal curvilinear coordinates (Yu et al., 2018). Therefore, the tripolar grid from Murray (1996) can be applied in CAS-LICOM3, with two North Poles, on the Eurasian (55°N, 95°E) and North American (55°N, 85°W) continents, respectively.

Second, the coupler was updated from NCAR flux coupler 6 to coupler 7 when the ocean component was coupled with the Community Ice Code, version 4 (CICE4). Also, it has been proved to be helpful for the high-resolution coupling (Lin et al., 2016).

Third, the central difference scheme is used in the momentum equations and the Leapfrog format with an Asselin filter is used for the time integration of the momentum equations. Additionally, the two-step preserving shape advection scheme (Yu, 1994; Xiao, 2006) and implicit vertical viscosity/diffusivity (Yu et al., 2018) were adopted for the tracer equations.

Fourth, with regard to the physical processes, the St. Laurent et al. (2002) internal tidal mixing scheme has been introduced into CAS-LICOM3 (Yu et al., 2017). The vertical viscosity and diffusion coefficients in the mixed layer are computed by the scheme of Canuto et al. (2001, 2002), with background values of 2×10^{-6} m^2 s^{-1} and upper limit of 2×10^{-2} m^2 s^{-1}. Besides, the chlorophyll-a dependent solar penetration of Ohlmann (2003) introduced by Lin et al. (2007) was also implemented in CAS-LICOM3.

2.2. *High-resolution experiment design*

The eddy-resolving simulation of CAS-LICOM3 (CAS-LICOM3_High) is forced by JRA55-do data (Tsujino et al., 2018), which were developed based on the JRA-55 product (Kobayashi et al., 2015). The temporal resolution of JRA55-do is 3-h and the horizontal resolution is 0.5625°. The atmospheric state variables and radiative fluxes are employed to compute the net surface flux into the ocean–sea-ice system in JRA55-do data, which included the air temperature at 10 m, the air density at 10 m, the relative humidity at 10 m, the surface wind vectors at 10 m, the sea surface pressure, the surface downward and upward shortwave flux, and the surface downward longwave flux (here, flux into the ocean is called "downward"). The turbulence heat and momentum fluxes of JRA55-do data have been computed using the bulk formula of Large and Yeager (2004). In the formula, the relative 10 m winds are employed and they are obtained by subtracting full ocean currents from the 10 m winds. The freshwater flux includes the precipitation (snow and rainfall) from JRA-55, as well as the continental runoff, which incorporates the runoff of ice sheets and glaciers from Greenland and Antarctica. The simulation is forced every 6 hours, even though the JRA55-do data are three-hourly, and integrated for 61 years from 1958 to 2018.

The experiment follows the OMIP-2 protocol, with the initial condition of the temperature and salinity from observation and a state of rest. The initial values in this study are different from the standard OMIP-2 experiment; they are the

temperature and salinity on 1 January 2014 from the Mercator Ocean analysis (Lellouche et al., 2018; Artana et al., 2019), not the World Ocean Atlas (Antonov et al., 2006, 2010; Locarnini et al, 2006, 2010). Meanwhile, the surface salinity is restored to the monthly Polar Science Center Hydrographic Climatology, version 3 (PHC3.0; Steele et al., 2001) over the entire domain with a salinity piston velocity of 50 m (4 yr)$^{-1}$ [plus 50 m (30 d)$^{-1}$ for the sea ice regions].

The horizontal grid contains 3600×2302 points with a resolution of approximately 1/10°, which is 11 km zonally and varies from 11 km at the equator to 8 km in midlatitudes and 2.7 km around the Antarctic. The higher resolution of CAS-LICOM3_High than the forcing data may imply that eddy-resolving activities come from the internally generated variability. The η-coordinate (Mesinger and Janjic, 1985) with 55 levels is applied in the vertical grid. The biharmonic scheme with a horizontal viscosity coefficient of -2.8×10^{10} m^4 s^{-1} is chosen in CAS-LICOM3_High. The full ocean surface velocity is used in the calculation of wind stress (relative wind stress), which can affect the strength of the North Equatorial Countercurrent (Sun et al., 2019, 2020).

2.3. *Methods*

To avoid the interference of the long-term trend and seasonal cycle when analyzing the temporal variations, the least-squares linear trend is first removed. Then, the de-seasonalized method is applied. The de-seasonalized method here means the removal of the climatological monthly mean from the detrended time series.

The STD here is calculated after removing the least-squares linear trend and the seasonal cycle. Also, the data from CAS-LICOM3_High are interpolated into a 25-km resolution when comparing with the observations or reanalysis data.

The spatial correlation coefficient calculated in this study is the Pearson product-moment coefficient of linear correlation between two datasets. For the Pearson correlation coefficient, the linear change of the two variables will not change the value of Pearson correlation. That is, high correlation does not mean two variables are exactly the same; rather, that they have the same spatial gradient.

The root-mean-square error (RMSE) of SST calculated in this study is also based on the model data interpolated to the observation grid. The formula is:

$$\text{RMSE} = \sqrt{\frac{\sum \left(\text{SST}_{\text{model},i} A_i - \text{SST}_{\text{obs},i} A_i\right)^2}{\sum A_i^2}} , \qquad (1)$$

where A_i stands for the area of each grid cell; and $\text{SST}_{\text{model}}$ and SST_{obs} are the simulated and observed SST, respectively.

A spatial filter method is used here, which is adopted from Bryan et al. (2010) and Lin et al. (2019), to extract the oceanic mesoscale signal. First, a filter box with 3° of longitude and 3° of latitude is used for monthly mean data to obtain the box-mean value as the lowpass-filtered value.

The value is considered as the large-scale signal. Second, the STDs of both daily SST and the lowpass-filtered monthly SST are calculated. Third, the difference between those two STDs is used to reflect the role of the mesoscale signal. In that way, the impact of the interannual variability of large-scale signals can be removed.

The eddy kinetic energy (EKE) computed here is the square of the temporal anomaly of the velocity (u' and v'), which is calculated based on the daily anomaly of SSH (η'). The formula is as follows:

$$\text{EKE} = \frac{1}{2}\left(u'^2 + v'^2\right) , \qquad (2)$$

$$u' = -\frac{g}{f}\frac{\partial \eta'}{\partial y} , \qquad (3)$$

$$v' = \frac{g}{f}\frac{\partial \eta'}{\partial x} , \qquad (4)$$

where g is gravity, f is the Coriolis parameter, and η' is the daily anomaly of SSH. η' is calculated by subtracting the climatological annual mean of the dataset.

3. Validation

3.1. *Temporal evolution*

The temporal evolutions of the annual mean globally averaged SST, SSS, AMOC, KE and temperature anomaly over the Niño3.4 index region from CAS-LICOM3_High are evaluated against the observation, reanalysis and the low-resolution experiment (CAS-LICOM3_Low; see details in Appendix A) (Fig. 1). The temporal evolution of the annual globally averaged SST is captured well by CAS-LICOM3_High (Fig. 1a). Here, three validated datasets have been applied, including the Extended Reconstructed SST, version 5 (ERSST.v5; resolution of 2°; Huang et al., 2017), Optimum Interpolation Sea Surface Temperature, version 2 (OISSTv2; resolution of 1/4°; Banzon et al., 2016; Reynolds et al., 2007), and SST from IAP (IAP_T; resolution of 1°; Cheng et al., 2015). An obvious warming trend of about 0.11°C (10 yr)$^{-1}$ can be seen during 1958–2018, and 0.13°C (10 yr)$^{-1}$ during 1982–2018, in CAS-LICOM3_High. The trends during the two periods are larger than those from ERSST.v5 and slightly smaller than those from OISSTv2. Compared with OISSTv2, the trends in CAS-LICOM3_High are better than those in CAS-LICOM3_Low, which may be related to the better simulation of both large-scale currents and mesoscale eddies in CAS-LICOM3_High. The STDs range from 0.06°C to 0.08°C for all simulations and observations, and the correlations are all higher than 0.9, as listed in Table 1. This suggests both the magnitude and phase of interannual–decadal variability in CAS-LICOM3_High match the observed one very well.

Figure 1b shows the time series of the global mean annual SSS from CAS-LICOM3_High, Argo data (http://doi.
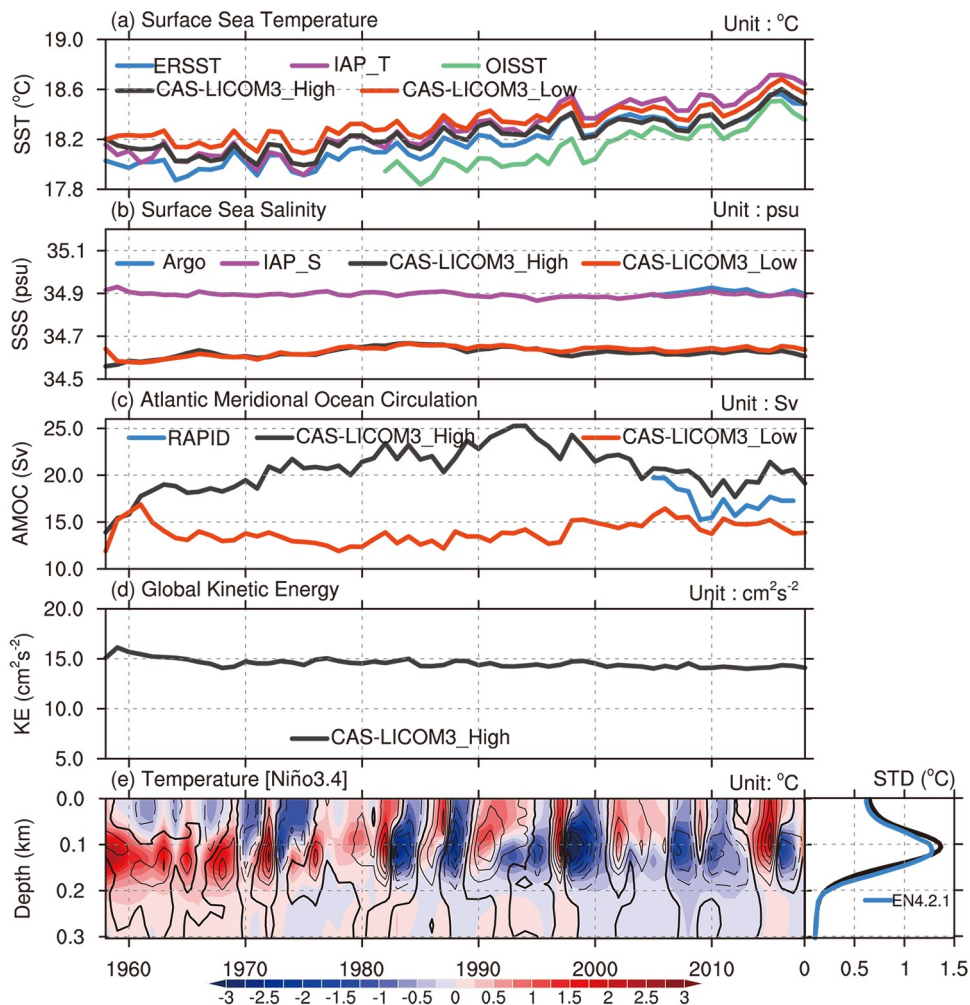
Fig. 1. Annual global mean (a) SST (unit: °C), (b) SSS (unit: psu), (c) AMOC (unit: Sv), and (d) global KE (unit: cm² s⁻²) during the whole cycle from 1958–2018. The left-hand panel of (e) is the depth–time section of the upper 300-m temperature anomaly averaged over the Niño3.4 region (5°N–5°S, 170°–120°W), with shading for CAS-LICOM3_High and contours for EN4.2.1 analyses. The thick lines refer to the 0°C isotherm. Dashed (solid) lines mean negative (positive) temperature anomalies. The right-hand panel of (e) shows the profiles of the annual temperature anomaly STDs for the EN4.2.1 dataset (cyan) and CAS-LICOM3_High (black). The annual mean data are used here.

org/10.17882/42182), and salinity data from IAP (IAP_S; Cheng et al., 2015). The values of the trends and STDs of the annual mean time series in CAS-LICOM3_High, Argo and IAP_S are all small (close to 0). The correlation coefficients of SSS between simulation and observation for both high- and low-resolution results are much lower than that of SST (Table 1), while the correlation coefficients between the two simulations are much higher. This indicates the large uncertainties in the surface freshwater fluxes. The mean values of SSS for the two experiments are smaller than those of observations, suggesting differences between the observational datasets and the model initial conditions.

The temporal evolution of AMOC is displayed in Fig. 1c. Compared with observation from RAPID (RAPID/MOCHA/ WBTS array; Cunningham et al., 2007), CAS-LICOM3_ High has a better simulation of AMOC evolution than CAS-LICOM3_Low. Although we cannot exactly figure out the reason for the improvement in CAS-LICOM3_High yet, the refined horizontal resolution does contribute to improving the simulation of the ocean large-scale circulations. The improvement of the mesoscale eddy, the location of the Gulf Stream and the deep convection area, and the heat and salinity budget in the upper mixed layer, are all possibly responsible for the improvement in the AMOC variation.

Figure 1d shows the evolution of the global mean KE from CAS-LICOM3_High during the whole integration period. The global KE increases quickly during first two years, and then decreases slowly in the next five or ten years. It finally keeps a steady state at values of around 15 cm² s⁻² in the following years. Therefore, the 61-year integration can reach a steady state for the global mean KE, but it may be not long enough for the deep circulation.

Figure 1e displays the time–depth section and STD profiles of the annual mean upper 300-m temperature anomaly averaged over the Niño3.4 region (5°N–5°S, 170°–120°W) from CAS-LICOM3_High and EN4.2.1 objective analyses

Table 1. Climatological annual mean (units: °C, psu, cm^2 s^{-2}), STD (units: °C, psu, cm^2 s^{-2}) and linear trend [units: °C (100 yr)$^{-1}$, psu (10 yr)$^{-1}$, cm^2 s^{-2} (10 yr)$^{-1}$] of SST, SSS and EKE during 1958–2018 from CAS-LICOM3_High, CAS-LICOM3_Low, and multiple observations. The temporal correlation coefficients of these variables between models and observations during the full period are also shown. The values in brackets represent the values during different periods. SST$_{1982}$, SSS$_{2005}$ and EKE$_{1993}$ represent the values during 1982–2018, 2005–2018 and 1993–2018, respectively.

Variables	Data	Annual Mean	STD	Linear Trend	Correlation (CAS-LICOM3_High)	Correlation (CAS-LICOM3_Low)
SST (SST$_{1982}$)	OISST	(18.15)	(0.07)	(0.15)	(0.93)	(0.93)
	ERSST	18.18 (18.29)	0.07 (0.06)	0.09 (0.11)	0.97 (0.95)	0.97 (0.95)
	IAP_T	18.29 (18.42)	0.08 (0.07)	0.07 (0.08)	0.96 (0.94)	0.96 (0.94)
	CAS-LICOM3_Low	18.33 (18.41)	0.07 (0.07)	0.07 (0.08)	0.99	–
	CAS-LICOM3_High	18.24 (18.32)	0.08 (0.07)	0.11 (0.13)	–	0.99
SSS (SSS$_{2005}$)	Argo	(34.91)	(0.01)	(0.00)	(0.23)	(0.37)
	IAP_S	34.89 (34.90)	0.01 (0.01)	−0.00 (−0.00)	−0.16 (0.50)	−0.16 (0.63)
	CAS-LICOM3_Low	34.63 (34.64)	0.02 (0.01)	0.00 (0.00)	0.79	–
	CAS-LICOM3_High	34.62 (34.62)	0.02 (0.01)	0.01 (0.01)	–	0.79
EKE (EKE$_{1993}$)	AVISO	(173.63)	(3.83)	(1.87)	(0.53)	–
	CAS-LICOM3_High	140.40 (147.60)	3.40 (2.42)	3.97 (6.15)	–	–

(Good et al., 2013). The close match of the temperature anomaly and the STD profiles between those two datasets indicates a good simulation of the interannual variability by CAS-LICOM3_High. The STDs of the annual mean SST anomaly over the Niño3.4 region are 0.65°C for CAS-LICOM3_High and 0.62°C for EN4.2.1. The temporal correlation coefficient of the annual mean SST anomaly over the Niño3.4 region between EN4.2.1 and CAS-LICOM3_High is significantly high (0.93). All these results indicate CAS-LICOM3_High can reproduce El Niño and La Niña events well. In addition, the warm temperature anomalies appear more frequently below the depth of 100 m before 1980 than they do after 1980. This phenomenon might be deserving of further research.

3.2. SSH and STD

The simulated spatial pattern of large-scale SSH from CAS-LICOM3_High is almost identical to the Archiving, Validation and Interpretation of Satellite Oceanographic Data (AVISO; http://www.aviso.altimetry.fr/), with a spatial correlation coefficient of 0.99 (Figs. 2a and b). In both CAS-LICOM3_High and AVISO, the high SSHs locate around the western boundary, and the low ones close to the eastern boundary, in the low and middle latitudes of the Pacific and Atlantic Ocean. The west–east contrast is associated with the easterly trade winds and the westward ocean currents. In the Indian Ocean, high SSH values are located in the east and low ones are in the west. In the high latitudes, the relatively low SSHs are located in the subpolar gyre in the Northern Hemisphere and south to the ACC in the Southern Ocean. This high spatial correlation between CAS-LICOM3_High and AVISO is expected, as the spatial correlation coefficient between AVISO and CAS-LICOM3_Low is also high.

Apart from the large-scale circulation, mesoscale eddies can also be reproduced in CAS-LICOM3_High. The amplitudes of mesoscale eddies are shown through the STD of the daily SSH anomaly from both AVISO and CAS-LICOM3_High (Figs. 2c and d). The high values of STD are presented in the western boundary currents (e.g., Kuroshio extension, Gulf Stream) and ACC, both for CAS-LICOM3_High and AVISO. There are also large STDs in the western and central tropical Pacific, which may be caused by the tropical instability waves (TIWs). The spatial correlation coefficient of the STD between AVISO and CAS-LICOM3_High is 0.93, which may be related to the eddy-resolving horizontal grid spacing of CAS-LICOM3_High.

Although the present resolution can resolve these western boundary currents well, it is still a challenge to simulate a correct separation owing to the sensitivity to the magnitude and formula of viscosity (Chassignet and Marshall, 2008). Thus far, we believe that the wrong separation location is related to the large viscosity in CAS-LICOM3_High. The biharmonic viscosity equation is employed with a viscosity coefficient of −2.8 × 10^{10} m^4 s^{-1} in the present experiment. In addition to the explicit viscosity, the Euler backward differences in the two-step shape preservation advection will provide additional numerical viscosity. Generally, the simulated amplitudes of eddy activities are underestimated compared with the observed ones, which is also shown and discussed in the time series of EKE later (Fig. 2e).

The temporal evolution of simulated EKE from CAS-LICOM3_High is compared with the value from AVISO, which has a horizontal resolution of 25 km, in Fig. 1e. Because the value from AVISO is available after October 1992, the statistics for both 1993–2018 and 1958–2018 are chosen and computed. The global annual mean EKE from CAS-LICOM3_High is underestimated by about 15%–20% compared with AVISO, which may be caused by the relat-
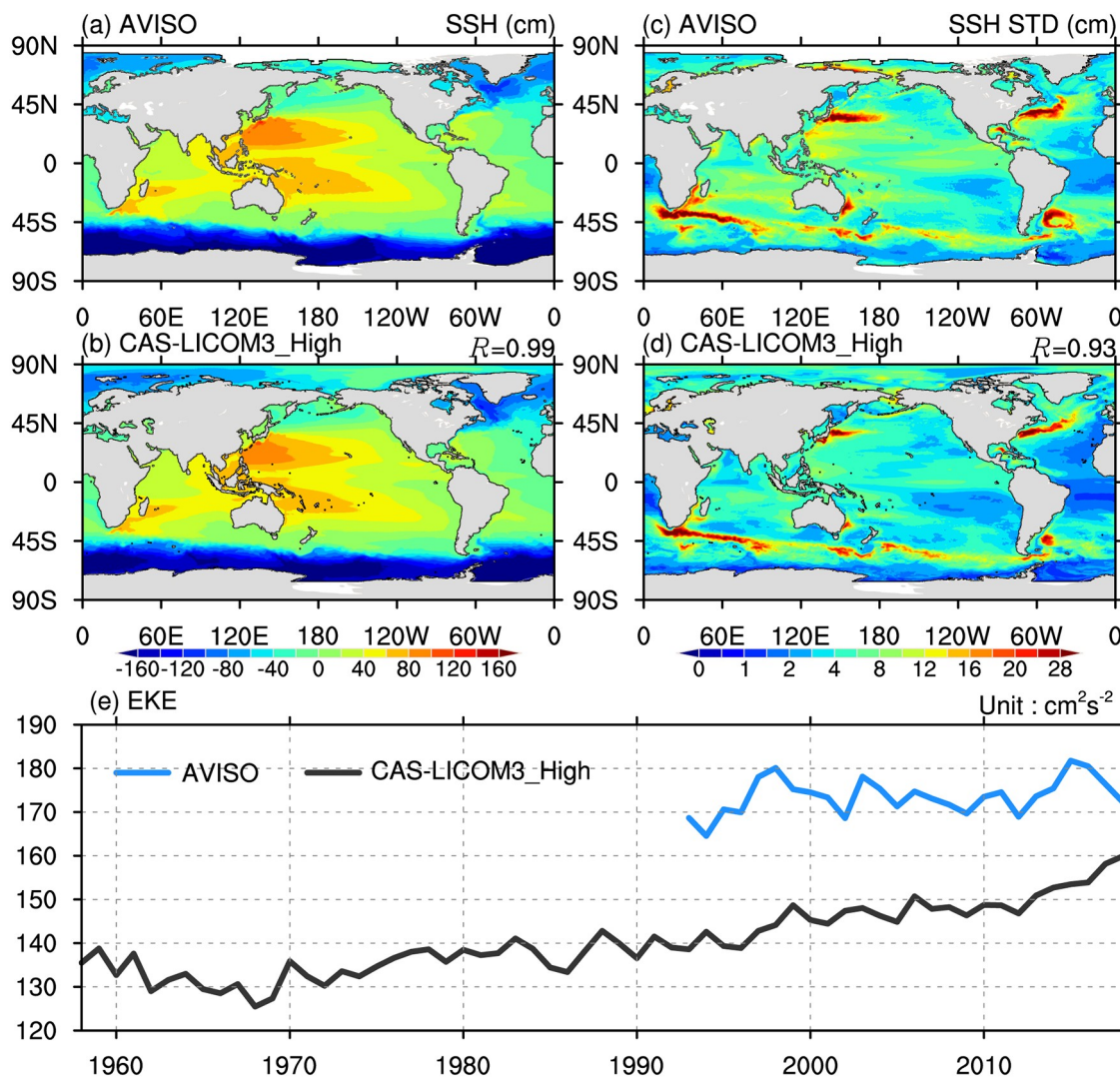
Fig. 2. (a) Climatological annual mean SSH (unit: cm) and (c) the STD of daily SSH from AVISO during 1993–2018. (b, d) As in (a, c) but for CAS-LICOM3_High. The pattern correlation coefficients (*R*) between AVISO and CAS-LICOM3_High are provided in the figures. (e) Annual global mean EKE (units: cm^2 s^{-2}) for CAS-LICOM3_High (black curves) and AVISO (cyan curves).

ively high viscosity or high numerical damping effects in CAS-LICOM3_High. The linear trend is overestimated during 1993–2018, with 6.15 cm^2 s^{-2} (10 yr)$^{-1}$ in CAS-LICOM3_High and 1.87 cm^2 s^{-2} (10 yr)$^{-1}$ in AVISO. The variability of observed EKE can be captured by CAS-LICOM3_High, with a temporal correlation coefficient of 0.53 during the same period. The magnitude of the variability of the simulated annual EKE is underestimated in CAS-LICOM3_High, as the STD is about 3.83 cm^2 s^{-2} for AVISO and 2.42 cm^2 s^{-2} for CAS-LICOM3_High.

3.3. *SST and STD*

The large-scale spatial features of SST are also simulated well by CAS-LICOM3_High (Figs. 3a and b), with a spatial correlation coefficient close to 1.0 between CAS-LICOM3_High and OISSTv2. We find that the meridional contrast of warm SST in the low latitudes and cold SST in the high latitudes, as well as the zonal contrast of the warm

pool [enclosed by the 28°C contour (thick blue line) in Fig. 3a] in the western Pacific and cold tongue in the eastern Pacific, are represented well in CAS-LICOM3_High. Also, the global RMSE is 0.47°C, which is smaller than that of CAS-LICOM3_low (0.59°C). The improvements of the SST simulation in these regions can mostly be attributed to the better simulation of the eddy transports in CAS-LICOM3_High than those in CAS-LICOM3_Low. For the Labrador Sea, the reduced bias may be related to convection processes, which have a correct location in CAS-LICOM3_High. However, in CAS-LICOM3_High, there are still larger biases in the regions over the western boundary, which may be caused by the bias of the simulation of the western boundary jet axes, as shown in Figs. 2 and 4.

The de-seasonalized STDs of the daily SST anomaly from OISSTv2 and CAS-LICOM3_High are shown in Figs. 3c and d. The spatial pattern of STDs is simulated well, with a global spatial correlation coefficient of 0.98 between
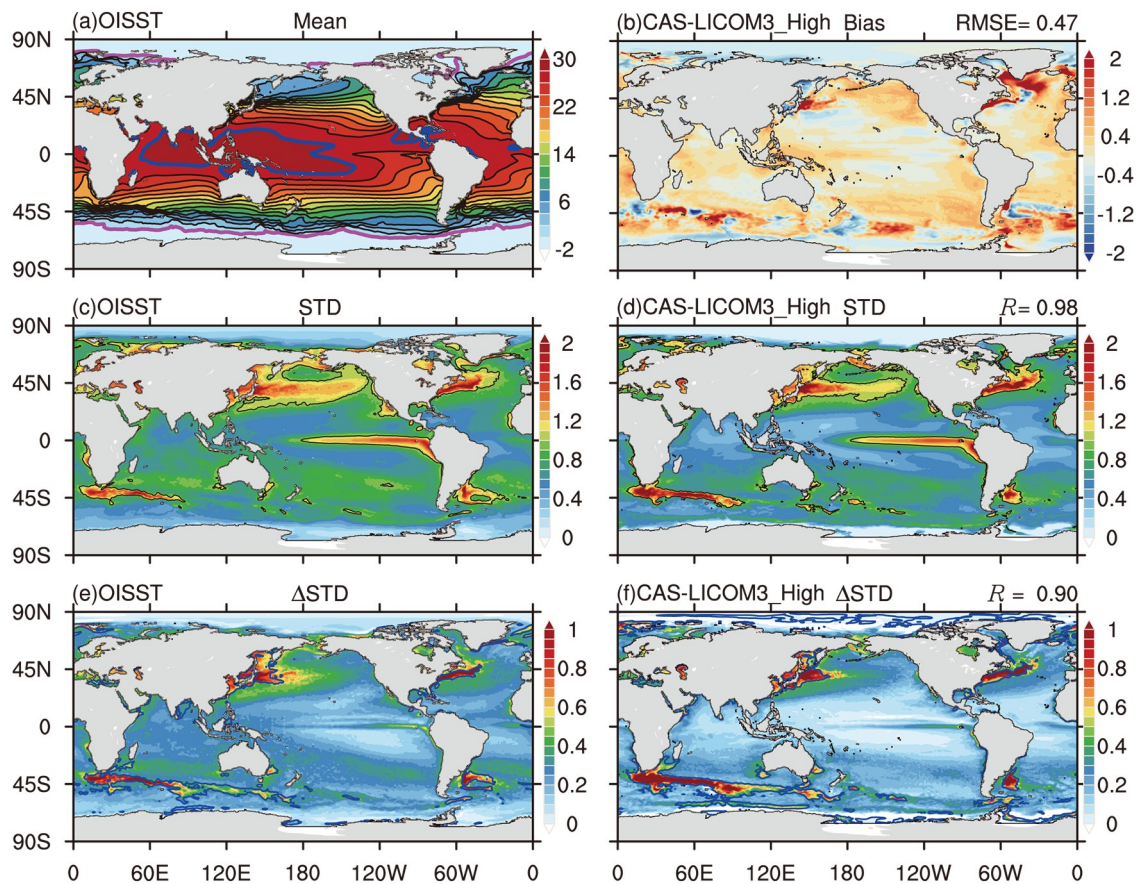
Fig. 3. Climatological annual mean SST (unit: °C) from (a) OISSTv2 and (b) the biases of CAS-LICOM3_High during 1982–2018 against OISSTv2. The blue and magenta lines in (a) are the 28°C and 0°C isotherms, respectively. (c, d) De-seasonalized STD of daily SST (STD; unit: °C) from (c) OISSTv2 and (d) CAS-LICOM3_High during 1982–2018. (e, f) As in (c, d) but for the ΔSTD by subtracting the STD of 3° × 3° low-pass filtered monthly SST from the STD of daily SST during 1982–2018. The black contours in (c, d) are the 1°C isotherms. The blue contours in (e, f) are the ratio of 0.5 between ΔSTD and STD. The RMSE and pattern correlation coefficients (*R*) between observation and CAS-LICOM3_High are also provided in the figures.

CAS-LICOM3_High and OISSTv2. The large STD values (> 1°C) are located in the equatorial Pacific, western boundary currents and their extensions, the Argentine Basin, and the Southern Ocean between the Indian Ocean and Atlantic Ocean. In the equatorial Pacific, the large STD is mainly due to the interannual variability associated with ENSO, and partly due to the intraseasonal variability related to eddy-induced TIWs. However, there are some underestimations of the simulated STD (Fig. 3d) over the warm SST regions (> 26°C contour lines in Fig. 3a).

Figures 3e and f show the difference between the daily SST STD and 3° × 3° lowpass-filtered monthly SST STD (ΔSTD). The difference indicates the variability due to the highpass signal related to mesoscale activities. As Figs. 3c and d show in the observation and CAS-LICOM3_High, large daily SST STDs are located in the eddy-rich regions, such as the western boundary and ACC. In those places, ΔSTD can reach 1°C (Figs. 3e and f). These large ΔSTD values are attributable to mesoscale eddies, which means the mesoscale signal can contribute to 50% of the total STD of daily SST (Figs. 3e and f). Meanwhile, in the eastern part of

the Pacific, mesoscale eddies can contribute to 20% of the STD in the observation and relatively less in CAS-LICOM3_High.

3.4. *Surface ocean currents*

The global large-scale surface current velocity during 1993–2018 for both the Ocean Surface Current Analyses Real-time (OSCAR; http://podaac.jpl.nasa.gov) dataset and CAS-LICOM3_High are shown in Fig. 4, with two western boundary regions zoomed in. The high speeds of the western boundary currents (such as the Kuroshio, Gulf Stream, North Brazil Current, etc.), equatorial current systems (including the South Equatorial Current, North Equatorial Countercurrent) and ACC, can be better represented in CAS-LICOM3_High than in CAS-LICOM3_Low.

For the western boundary currents, the simulated Kuroshio path flows along the shelf break inside the East China Sea between Taiwan Island and Yonaguni-jima Island, which is also proven by observations and other numerical simulations (Johns et al., 2001; Yang et al., 2012). The Gulf Stream in CAS-LICOM3_High can extend to 40°W, but it
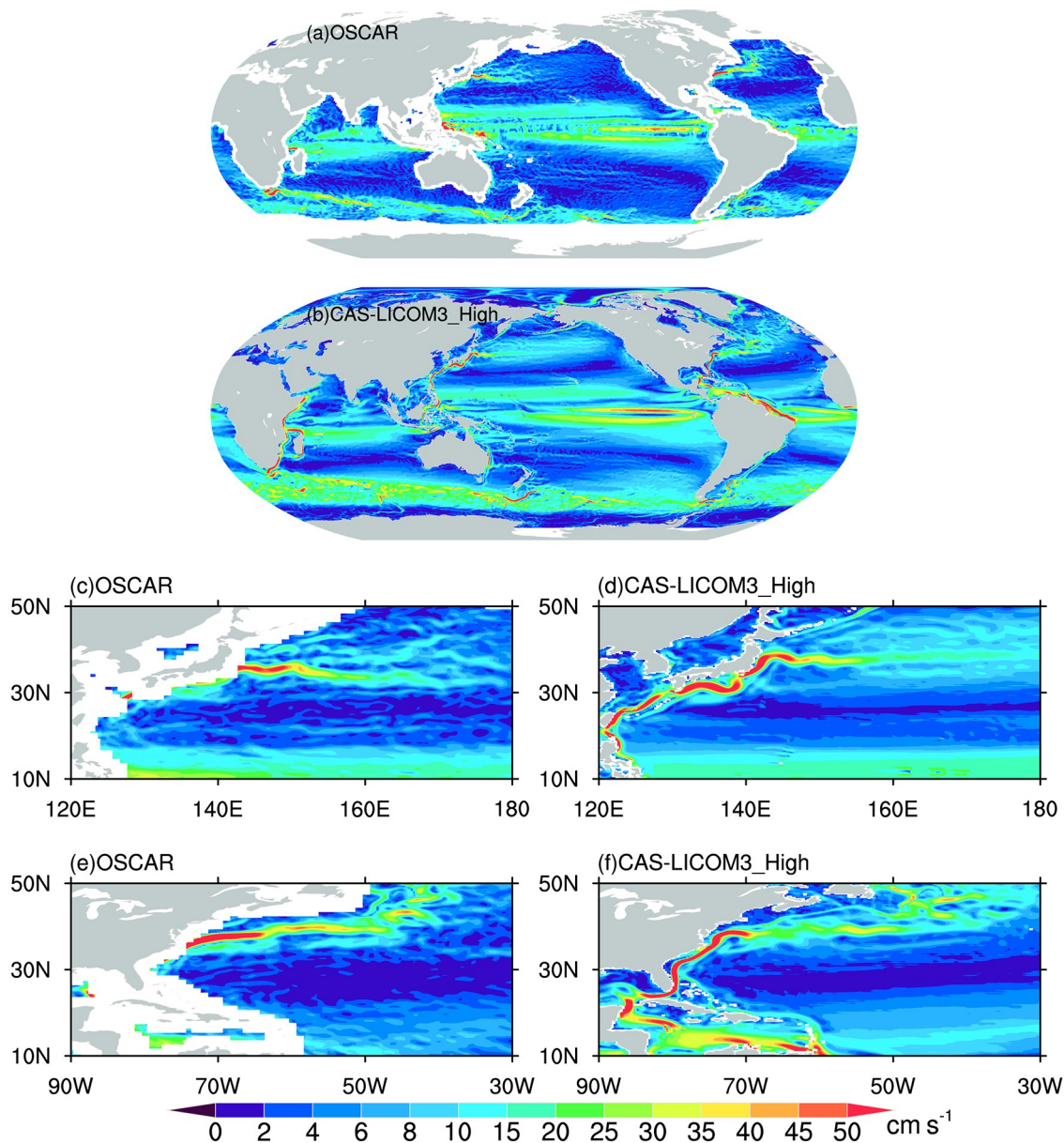
Fig. 4. Climatological annual mean velocity of ocean surface currents from OSCAR during 1993–2018 for the (a) global, (c) Kuroshio and its extension, and (e) Gulf Stream regions. (b, d, f) As in (a, c, e) but from CAS-LICOM3_High (units: cm s^{-1}).

does not extend as a coherent feature past the New England seamounts, which is also exhibited in the 1/25° simulation from Chassignet and Xu (2017). However, there is a bias about the western boundary currents, as the separation of both the Kuroshio and Gulf Stream shifts northward by about 2° of latitude, compared with OSCAR.

3.5.   NEUC

The zonal belt structure of the zonal currents are important features for the global ocean, which also cannot be simulated by coarse-resolution models. As discussed in Li et al. (2018), the simulation of the NEUC requires both a high-resolution and long-term simulation, thus meaning the NEUC is a good metric to evaluate high-resolution and long-term simulations. As presented in Fig. 5, the meridional sections

of zonal velocity averaged over 135°–140°E, 175°–180°E, and 150°–145°W, from 11-year mean Argo data (Roemmich and Gilson, 2009) and CAS-LICOM3_High, show three branches of NEUCs (Qiu et al., 2013), in all three meridional sections. The Argo zonal velocities are estimated from the density gradients calculated based on the observed temperature and salinity. The upper boundary of the three NEUC jets for CAS-LICOM3_High become deeper with increasing latitude and shallower from west to east, which is exactly the same as in Argo. Although the locations of the NEUC jets are reproduced very well by CAS-LICOM3_High, their strength in CAS-LICOM3_High is weaker than in Argo, which may be related to the non-geostrophic velocity (Li et al., 2018) or the relatively large viscosity in the model.

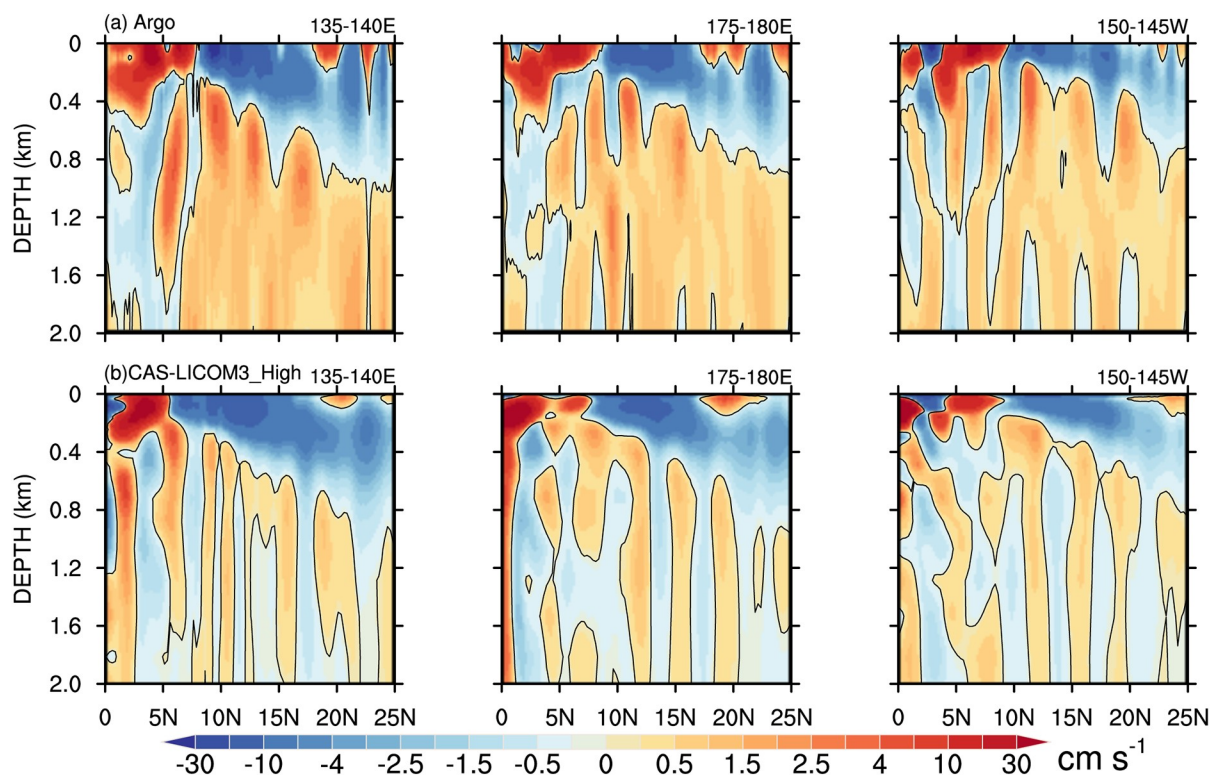In summary, CAS-LICOM3_High can reproduce well

Fig. 5. (a) The 11-year mean zonal velocity (shading; units: cm s^{-1}) averaged over 135°–140°E (left), 175°–180°E (middle), and 150°–145°W (right) for Argo during 2004–2014. (b) As in (a) but for CAS-LICOM3_High. The zero contours are shown as solid contours.

the long-term trend and interannual–decadal variability of various variables. The refined resolution simulation can not only capture the mesoscale eddies, the western boundary currents, and the zonal jets, but also improve the representation of large-scale circulations. In addition, the mesoscale activities can affect the magnitude of the variabilities, as the mesoscale signal is responsible for up to 50% of the variability of daily SST in eddy-rich regions. The processes related to these variabilities can be further investigated using this dataset and the added value of the high resolution can also be evaluated by comparing with the low-resolution simulation, particularly where the biases have been significantly reduced. In addition, this preliminary evaluation also indicates some systematic biases in the global temperature and salinity, the EKE, and regional current patterns. We will further improve the model in the future.

4. Data records

An eddy-resolving dataset of CAS-LICOM3_High for OMIP-2 has been uploaded to the ESGF node and can be found at https://esgf-node.llnl.gov/projects/cmip6/. Although the model outputs are unformatted with big-endianness and double precision, we converted all the variables into NetCDF, version 4, and single precision for analysis. These data can be easily handled by common computer programming languages and professional software, such as Climate Data Operators (https://code.mpimet.mpg.de/projects/cdo/) or NetCDF Operator (http://nco.sourceforge.net).

5. Usage notes

The original model outputs are on a tripolar grid with two poles at (55°N, 95°E) and (55°N, 85°W) in the Northern Hemisphere continent. There are 3600 and 2302 grid numbers in the zonal and meridional directions of the horizontal domain, respectively. The dataset was interpolated to a 1/4° latitude–longitude rectangular grid via the first-order conservation interpolation method for ease of analysis. The dataset has 55 vertical levels, which is the original vertical level, and has not changed on ESGF nodes. The detail of each vertical level can be found in Appendix B, Table B.

There are 23 variables and 4 parameters provided in this dataset, including daily and monthly SSS, SST and SSH. The monthly three-dimensional ocean temperature, salinity and ocean velocities are also included. The monthly global mean temperature, salinity and AMOC are also uploaded in the dataset. Information on the data grid, such as area, mask, cell thickness and volume for every ocean grid, is also provided. The detail of each variable can be found in Appendix C, Table C.

APPENDIX A

DESCRIPTION OF CAS-LICOM3_LOW

This appendix describes the experiment design of CAS-LICOM3_Low and compares it with CAS-LICOM3_High.

CAS-LICOM3_Low shares most settings with CAS-LICOM3_High, but there are some differences. First, CAS-

Table A. Comparison between CAS-LICOM3_High and CAS-LICOM3_Low.

	CAS-LICOM3_High	CAS-LICOM3_Low
Horizontal grid spacing	1/10° (11 km in longitude, about 11 km at the equator, and 8 km at midlatitudes)	1° (110 km in longitude, about 110 km at the equator, and 80 km at midlatitudes)
Explicit horizontal viscosity	Biharmonic $A_4 = -2.8 \times 10^{10}$ m^4 s^{-1}	Laplacian $A_2 = 5400$ m^2 s^{-1}
Explicit vertical viscosity	Background viscosity of 2×10^{-6} m^2 s^{-1} in Canuto et al. (2001, 2002) with upper limit of 2×10^{-2} m^2 s^{-1}	Background viscosity of 2×10^{-6} m^2 s^{-1} in Canuto et al. (2001, 2002) with upper limit of 2×10^{-2} m^2 s^{-1}
Explicit Horizontal diffusivity	Biharmonic $A_4 = -2.8 \times 10^{10}$ m^2 s^{-1}	Laplacian $A_2 = 5400$ m^2 s^{-1}
Explicit vertical diffusivity	Background viscosity of 2×10^{-6} m^2 s^{-1} in Canuto et al. (2001, 2002) with upper limit of 2×10^{-2} m^2 s^{-1}	Background viscosity of 2×10^{-6} m^2 s^{-1} in Canuto et al. (2001, 2002) with upper limit of 2×10^{-2} m^2 s^{-1}
Isopycnal scheme, e.g., GM	No GM and Redi, Biharmonic $A_4 = -2.8 \times 10^{10}$ m^4 s^{-1}	Both Redi and GM with the same coefficient computed by Ferreira et al. (2005)
Mixed layer scheme	Canuto et al. (2001, 2002)	Canuto et al. (2001, 2002)
Advection scheme	Leapfrog for momentum; two step preserved shape advection scheme for tracer (Yu, 1994)	Leapfrog for momentum; two step preserved shape advection scheme for tracer (Yu, 1994)
Time stepping scheme	Split-explicit Leapfrog with Asselin filter (0.2 for barotropic; 0.43 for baroclinic; 0.43 for tracer)	Split-explicit Leapfrog with Asselin filter (0.2 for barotropic; 0.43 for baroclinic; 0.43 for tracer)
Bottom drag	$C_b = 2.6 \times 10^{-3}$	$C_b = 2.6 \times 10^{-3}$
Surface wind-stress	Absolute wind stress	Absolute wind stress
Vertical coordinates	55 η levels	30 η levels
SSS restoring	50 m (4 yr)$^{-1}$; 50 m (30 d)$^{-1}$ for sea-ice region	50 m (4 yr)$^{-1}$; 50 m (30 d)$^{-1}$ for sea-ice region

LICOM3_Low uses the PHC3.0 temperature and salinity as the initial state. In CAS-LICOM3_Low, the Laplacian scheme was used, which is different from the biharmonic scheme in CAS-LICOM3_High. The biharmonic scheme has the so-called "scale selected" feature. It is more effective to damp the checkerboard noise than the Laplacian scheme. Therefore, the resolved scales are less damped. This is good for the simulation of the mesoscale eddies.

The coupled CICE4 in CAS-LICOM3_Low contains both dynamic and thermodynamic sea-ice processes, while only the thermodynamic process of CICE4 is coupled in CAS-LICOM3_High. The lack of dynamic sea ice can lead to bias in the Arctic, especially for sea-ice volume. A detailed description of the low-resolution dataset can be found in Lin et al. (2020). Table A compares the parameters from CAS-LICOM3_Low and CAS-LICOM3_High.

APPENDIX B

DEPTH OF MODEL LEVELS FOR *T*- AND *W*-GRID

Table B. Depth of model levels for *T*- and *W*-grid.

Level	*T*-grid	*W*-grid
1	2.50	0.00
2	7.51	5.00
3	12.56	10.02
4	17.67	15.10
5	22.86	20.24
6	28.15	25.48
7	33.57	30.83
8	39.14	36.32
9	44.87	41.96
10	50.79	47.78
11	56.90	53.79
12	63.22	60.01
13	69.76	66.44
14	76.54	73.09
15	83.55	79.98
16	90.81	87.12
17	98.31	94.49
18	106.05	102.12
19	114.04	109.98
20	122.26	118.09
21	130.72	126.44

Table B. (Continued.)

Level	T-grid	W-grid
22	139.40	135.01
23	148.29	143.79
24	157.37	152.78
25	166.64	161.96
26	176.07	171.32
27	185.65	180.83
28	195.36	190.48
29	205.17	200.24
30	215.06	210.10
31	225.01	220.02
32	235.00	230.00
33	245.00	240.00
34	257.08	250.00
35	275.35	264.15
36	303.81	286.54
37	346.28	321.09
38	406.31	371.48
39	487.12	441.14
40	591.53	533.09
41	721.96	649.98
42	880.31	793.95
43	1067.98	966.68
44	1285.80	1169.28
45	1534.07	1402.32
46	1812.49	1665.81
47	2120.22	1959.17
48	2455.88	2281.28
49	2817.55	2630.48
50	3202.83	3004.62
51	3608.89	3401.05
52	4032.51	3816.78
53	4470.13	4248.28
54	4917.95	4691.98
55	5371.96	5143.91
56		5600.00

APPENDIX C

DESCRIPTION OF DATASET VARIABLES

Table C. Description of dataset variables.

Name	Description	Horizontal resolution	Vertical resolution	Frequency
mlotst	Ocean mixed-layer thickness defined by sigma-T	25 km	1 layer	Monthly
msftmz	Ocean meridional overturning mass streamfunction	50 km	55 layers	Monthly
so	Seawater salinity	25 km	55 layers	Monthly
soga	Global mean seawater salinity	–	–	Monthly
sos	Sea surface salinity	25 km	1 layer	Monthly
sosga	Global average sea surface salinity	–	–	Monthly
thetao	Seawater potential temperature	25 km	55 layers	Monthly
thetaoga	Global average seawater potential temperature	–	–	Monthly
tos	Sea surface temperature	25 km	1 layer	Monthly
tosga	Global average sea surface temperature	–	–	Monthly
uo	Seawater X-velocity	25 km	55 layers	Monthly
vo	Seawater Y-velocity	25 km	55 layers	Monthly
wo	Seawater vertical velocity	25 km	55 layers	Monthly
zos	Sea surface height above geoid	25 km	1 layer	Monthly
tob	Seawater potential temperature at sea floor	25 km	1 layer	Monthly

Table C. (Continued.)

Name	Description	Horizontal resolution	Vertical resolution	Frequency
sob	Seawater salinity at sea floor	25 km	1 layer	Monthly
amoc_rapid	Mean max AMOC at 26°N	–	–	Monthly
smoc	Mean at 34°S for maximum streamfunction for AMOC	–	–	Monthly
mfo_drake	Monthly Drake Passage transport	–	–	Monthly
mfo_indo	Monthly Indonesian Throughflow transport	–	–	Monthly
sos	Sea surface salinity	25 km	1 layer	Daily
tos	Sea surface temperature	25 km	1 layer	Daily
zos	Sea surface height above geoid	25 km	1 layer	Daily
areacello	Grid-cell area for ocean variables	25 km	1 layer	Fixed
deptho	Sea floor depth below geoid	25 km	–	Fixed
thkcello	Ocean model cell thickness	25 km	55 layers	Fixed
volcello	Ocean grid-cell volume	25 km	55 layers	Fixed

Data availability statement

The data that support the findings of this study are available from https://esgf-node.llnl.gov/projects/cmip6/. The citation is "*CAS FGOALS-f3-H model output prepared for CMIP6 OMIP version2*. Earth System Grid Federation. http://doi.org/10.22033/ESGF/CMIP6.13283".

Disclosure statement

No potential conflict of interest was reported by the authors.

REFERENCES

Antonov, J. I., and Coauthors, 2010: *World Ocean Atlas 2009, Volume 2: Salinity*. U.S. Government Printing Office.

Antonov, J. I., R. A. Locarnini, T. P. Boyer, A. V. Mishonov, and H. E. Garcia, 2006: *World Ocean Atlas 2005, Volume 2: Salinity*. U.S. Government Printing Office.

Artana, C., and Coauthors, 2019: Twenty-five years of Mercator ocean reanalysis GLORYS12 at Drake Passage: Velocity assessment and total volume transport. Advances in Space Research, https://doi.org/10.1016/j.asr.2019.11.033.

Banzon, V., T. M. Smith, T. M. Chin, C. Y. Liu, and W. Hankins, 2016: A long-term record of blended satellite and in situ sea-surface temperature for climate monitoring, modeling and environmental studies. *Earth System Science Data*, **8**, 165−176, https://doi.org/10.5194/essd-8-165-2016.

Bryan, F. O., R. Tomas, J. M. Dennis, D. B. Chelton, N. G. Loeb, and J. L. McClean, 2010: Frontal scale air-sea interaction in high-resolution coupled climate models. *Journal of Climate*, **23**(23), 6277−6291, https://doi.org/10.1175/2010JCLI3665.1.

Canuto, V. M., A. Howard, Y. Cheng, and M. S. Dubovikov, 2001: Ocean turbulence. Part I: One-point closure model—Momentum and heat vertical diffusivities. *J. Phys. Oceanogr.*, **31**, 1413−1426, https://doi.org/10.1175/1520-0485(2001)031<1413:OTPIOP>2.0.CO;2.

Canuto, V. M., A. Howard, Y. Cheng, and M. S. Dubovikov, 2002: Ocean turbulence. Part II: Vertical diffusivities of momentum, heat, salt, mass, and passive scalars. *J. Phys. Oceanogr.*, **32**, 240−264, https://doi.org/10.1175/1520-0485(2002)032<0240:OTPIVD>2.0.CO;2.

Chassignet, E. P., and D. P. Marshall, 2008: Gulf Stream separation in numerical ocean models. *Ocean Modeling in an Eddying Regime*, M. W. Hecht and H. Hasumi, Eds., *Geophys. Monogr.*, Vol. 177, Amer. Geophys. Union, 39-62, https://doi.org/10.1029/177GM05.

Chassignet, E. P., and X. B. Xu, 2017: Impact of horizontal resolution (1/12° to 1/50°) on gulf stream separation, penetration, and variability. *J. Phys. Oceanogr.*, **47**, 1999−2021, https://doi.org/10.1175/JPO-D-17-0031.1.

Chassignet, E. P., and Coauthors, 2020: Impact of horizontal resolution on global ocean-sea-ice model simulations based on the experimental protocols of the Ocean Model Intercomparison Project phase 2(OMIP-2). *Geoscientific Model Development*, https://doi.org/10.5194/gmd-2019-374.

Cheng, L.-J., C., J. Zhu, and J. Abraham, 2015: Global upper ocean heat content estimation: Recent progress and the remaining challenges. *Atmos. Ocean. Sci. Lett.*, **8**, 333−338, https://doi.org/10.3878/AOSL20150031.

Cunningham, W. A., P. D. Zelazo, D. J. Packer, and J. J. Van Bavel, 2007: The iterative reprocessing model: A multilevel framework for attitudes and evaluation. *Social Cognition*, **25**, 736−760, https://doi.org/10.1521/soco.2007.25.5.736.

Ferreira, D., J. Marshall, and P. Heimbach, 2005: Estimating eddy stresses by fitting dynamics to observations using a resid-

ual-mean ocean circulation model and its adjoint. *J. Phys. Oceanogr.*, **35**, 1891−1910, https://doi.org/10.1175/JPO 2785.1.

Good, S. A., M. J. Martin, and N. A. Rayner, 2013: EN4: Quality controlled ocean temperature and salinity profiles and monthly objective analyses with uncertainty estimates. *J. Geophys. Res.: Oceans*, **118**, 6704−6716, https://doi.org/10.1002/2013JC009067.

Griffies, S. M., and Coauthors, 2016: OMIP contribution to CMIP6: Experimental and diagnostic protocol for the physical component of the Ocean Model Intercomparison Project. *Geoscientific Model Development*, **9**, 3231−3296, https://doi.org/10.5194/gmd-9-3231-2016.

Huang, B. Y., and Coauthors, 2017: Extended Reconstructed Sea Surface Temperature, Version 5 (ERSSTv5): Upgrades, Validations, and Intercomparisons. *J. Climate*, **30**, 8179−8205, https://doi.org/10.1175/JCLI-D-16-0836.1.

Johns, W. E., T. N. Lee, D. X. Zhang, R. Zantopp, C.-T. Liu, and Y. Yang, 2001: The Kuroshio East of Taiwan: Moored transport observations from the WOCE PCM-1 array. *J. Phys. Oceanogr.*, **31**, 1031−1053, https://doi.org/10.1175/1520-0485(2001)031<1031:TKEOTM>2.0.CO;2.

Kalnay, E., and Coauthors, 1996: The NCEP/NCAR 40-year reanalysis project. *Bull. Amer. Meteor. Soc.*, **77**, 437−472, https://doi.org/10.1175/1520-0477(1996)077<0437:TNYRP>2.0.CO;2.

Kistler, R., and Coauthors, 2001: The NCEP-NCAR 50-year reanalysis: Monthly means CD-ROM and documentation. *Bull. Amer. Meteor. Soc.*, **82**, 247−268, https://doi.org/10.1175/1520-0477(2001)082<0247:TNNYRM>2.3.CO;2.

Kobayashi, S., and Coauthors, 2015: The JRA-55 reanalysis: General specifications and basic characteristics. *J. Meteor. Soc. Japan.*, **93**, 5−48, https://doi.org/10.2151/jmsj.2015-001.

Large, W. G., and S. G. Yeager, 2004: Diurnal to Decadal Global Forcing for Ocean and Sea-Ice Models: The Data Sets and Flux Climatologies. NCAR Tech. Note: NCAR/TN-460+STR, CGD Division of the National Center for Atmospheric Research.

Large, W. G., and S. G. Yeager, 2009: The global climatology of an interannually varying air-sea flux data set. *Climate Dyn.*, **33**, 341−364, https://doi.org/10.1007/s00382-008-0441-3.

Lellouche, Jean-Michel, Eric Greiner, Olivier Le Galloudec, Gilles Garric and Charly Regnier., 2018: Recent updates to the Copernicus Marine Service global ocean monitoring and forecasting real-time 1/12° high-resolution system. *Ocean Sci*, **14**, 1093−1126, https://doi.org/10.5194/os-14-1093-2018.

Li, Y. W., H. L. Liu, and P. F. Lin, 2018: Interannual and decadal variability of the North Equatorial Undercurrents in an eddy-resolving ocean model. *Scientific Reports*, **8**, 17112, https://doi.org/10.1038/s41598-018-35469-2.

Lin, P. F., H. L. Liu, J. Ma, and Y. W. Li, 2019: Ocean mesoscale structure-induced air-sea interaction in a high-resolution coupled model. *Atmos. and Ocean. Sci. Lett.*, **12**(2), 98−106.

Lin, P. F., and Coauthors, 2016: A coupled experiment with LICOM2 as the Ocean component of CESM1. *J. Meteor. Res.*, **30**, 76−92, https://doi.org/10.1007/s13351-015-5045-3.

Lin, P. F., and Coauthors, 2020: LICOM model datasets for the CMIP6 Ocean model intercomparison project. *Adv. Atmos. Sci.*, **37**, 239−249, https://doi.org/10.1007/s00376-019-9208-5.

Lin, P. F., H. L. Liu, and X. H. Zhang, 2007: Sensitivity of the upper ocean temperature and circulation in the equatorial pacific to solar radiation penetration due to phytoplankton. *Adv. Atmos. Sci.*, **24**, 765−780, https://doi.org/10.1007/s00376-007-0765-7.

Liu, H. L., P. F. Lin, Y. Q. Yu, and X. H. Zhang, 2012: The baseline evaluation of LASG/IAP climate system ocean model (LICOM) version 2. *Acta Meteorologica Sinica*, **26**, 318−329, https://doi.org/10.1007/s13351-012-0305-y.

Liu, H. L., X. H. Zhang, W. Li, Y. Q. Yu, and R. C. Yu, 2004: An eddy-permitting oceanic general circulation model and its preliminary evaluation. *Adv. Atmos. Sci.*, **21**, 675−690, https://doi.org/10.1007/BF02916365.

Locarnini, R. A., A. V. Mishonov, J. I. Antonov, T. P. Boyer, and H. E. Garcia, 2006: *World Ocean Atlas 2005*, Vol. 1, *Temperature*. NOAA Atlas NESDIS 61, NOAA, U.S. Government Printing Office, Washington D.C.

Locarnini, R. A., A. V. Mishonov, J. I. Antonov, T. P. Boyer, H. E. Garcia, O. K. Baranova, M. M. Zweng, and D. R. Johnson, 2010: *World Ocean Atlas 2009*, Vol. 1, *Temperature*. NOAA Atlas NESDIS 68, NOAA, U.S. Government Printing Office.

Mesinger, F., and Z. I. Janjic, 1985: Problems and numerical methods of the incorporation of mountains in atmospheric models. *Large-Scale Computations in Fluid Mechanics, Part 2*, C. La Jolla, Ed., Lectures in Applied Mathematics, 81−120.

Murray, R. J., 1996: Explicit generation of orthogonal grids for ocean models. *J. Comput. Phys.*, **126**, 251−273, https://doi.org/10.1006/jcph.1996.0136.

Ohlmann, J. C., 2003: Ocean radiant heating in climate models. *J. Climate*, **16**, 1337−1351, https://doi.org/10.1175/1520-0442-16.9.1337.

Qiu, B., D. L. Rudnick, S. M. Chen, and Y. Kashino, 2013: Quasi-stationary North Equatorial Undercurrent jets across the tropical North Pacific Ocean. *Geophys. Res. Lett.*, **40**, 2183−2187, https://doi.org/10.1002/grl.50394.

Reynolds, R. W., T. M. Smith, C. Y. Liu, D. B. Chelton, K. S. Casey, and M. G. Schlax, 2007: Daily high-resolution-blended analyses for sea surface temperature. *J. Climate*, **20**, 5473−5496, https://doi.org/10.1175/2007JCLI1824.1.

Roemmich, D., and J. Gilson, 2009: The 2004-2008 mean and annual cycle of temperature, salinity, and steric height in the global ocean from the Argo Program. *Progress in Oceanography*, **82**, 81−100, https://doi.org/10.1016/j.pocean.2009.03.004.

St. Laurent, L. C., H. L. Simmons, and S. R. Jayne, 2002: Estimating tidally driven mixing in the deep ocean. *Geophys. Res. Lett.*, **29**, 21-1−21-4, https://doi.org/10.1029/2002GL015633.

Steele, M., R. Morley, and W. Ermold, 2001: PHC: A global ocean hydrography with a high-quality Arctic Ocean. *J. Climate*, **14**, 2079−2087, https://doi.org/10.1175/1520-0442(2001)014<2079:PAGOHW>2.0.CO;2.

Sun, Z. H., H. L. Liu, P. F. Lin, Z. P. Yu, and Y. W. Li, 2020: The simulation bias analysis of pacific North Equatorial countercurrent in LICOM3.0. *Chinese Journal of Atmospheric Sciences*, https://doi.org/10.3878/j.issn.1006-9895.1907.19123. (in Chinese with English abstract)

Sun, Z. K., H. L. Liu, P. F. Lin, Y.-H. Tseng, J. Small, and F. Bryan, 2019: The modeling of the North Equatorial countercurrent in the community earth system model and its oceanic component. *Journal of Advances in Modeling Earth Sys-*

tems, **11**, 531−544, https://doi.org/10.1029/2018MS001521.

Tsujino, H., and Coauthors, 2018: JRA-55 based surface dataset for driving ocean-sea-ice models (JRA55-do). *Ocean Modelling*, **130**, 79−139, https://doi.org/10.1016/j.ocemod.2018.07.002.

Tsujino, H., and Coauthors, 2020: Evaluation of global ocean–sea-ice model simulations based on the experimental protocols of the Ocean Model Intercomparison Project phase 2(OMIP-2). *Geoscientific Model Development*, https://doi.org/10.5194/gmd-2019-363.

Xiao, C., 2006: Adoption of a two-step shape-preserving advection scheme in an OGCM and its coupled experiment. M.S. thesis, Institute of Atmospheric Physics, Chinese Academy of Sciences, 89 pp. (in Chinese)

Yang, D. Z., B. S. Yin, Z. L. Liu, T. Bai, J. F. Qi, and H. Y. Chen, 2012: Numerical study on the pattern and origins of Kuroshio branches in the bottom water of southern East China Sea in summer. *J. Geophys. Res.: Oceans*, **117**, C02014, https://doi.org/10.1029/2011JC007528.

Yu, R. C., 1994: A two-step shape-preserving advection scheme. *Adv. Atmos. Sci.*, **11**, 479−490, https://doi.org/10.1007/BF02658169.

Yu, Y. Q., S. L. Tang, H. L. Liu, P. F. Lin, and X. L. Li, 2018: Development and evaluation of the dynamic framework of an ocean general circulation model with arbitrary orthogonal curvilinear coordinate. *Chinese Journal of Atmospheric Sciences*, **42**, 877−889, https://doi.org/10.3878/j.issn.1006-9895.1805.17284. (in Chinese with English abstract)

Yu, Z. P., H. L. Liu, and P. F. Lin, 2017: A numerical study of the influence of tidal mixing on Atlantic meridional overturning circulation (AMOC) Simulation. *Chinese Journal of Atmospheric Sciences*, **41**, 1087−1100, https://doi.org/10.3878/j.issn.1006-9895.1702.16263.

Zhang, X. H., and X. Z. Liang, 1989: A numerical world ocean general circulation model. *Adv. Atmos. Sci.*, **6**, 44−61, https://doi.org/10.1007/BF02656917.